Multi-Scale Fractal Analysis of Image Texture and Pattern

Charles W. Emerson, Nina Siu-Ngan Lam, and Dale A. Quattrochi

Abstract

Analyses of the fractal dimension of Normalized Difference Vegetation Index (NDVI) images of homogeneous land covers near Huntsville, Alabama revealed that the fractal dimension of an image of an agricultural land cover indicates greater complexity as pixel size increases, a forested land cover gradually grows smoother, and an urban image remains roughly self-similar over the range of pixel sizes analyzed (10 to 80 meters). A similar analysis of Landsat Thematic Mapper images of the East Humboldt Range in Nevada taken four months apart show a more complex relation between pixel size and fractal dimension. The major visible difference between the spring and late summer NDVI images is the absence of high elevation snow cover in the summer image. This change significantly alters the relation between fractal dimension and pixel size. The slope of the fractal dimension-resolution relation provides indications of how image classification or feature identification will be affected by changes in sensor spatial resolution.

Introduction

For as long as computers have been used to analyze geographical data sets, spatial data have placed heavy demands on the data processing and storage capabilities of hardware and software. As the geographical and temporal coverage, the spectral and spatial resolution, and the number of individual sensors increase, the sheer volume and complexity of available data sets will continue to tax hardware and software. The increasing importance of networking with the requirement to move data sets between different servers and clients makes the data volume problem particularly acute. Analytical techniques such as stochastic simulation, wavelet decomposition of images into different space and scale components, and geostatistics, which all require large amounts of storage as well as fast processors and networks, also tax available hardware, software, and network services. Mitigating this problem requires using data efficiently, that is, using data at the appropriate scale and resolution to adequately characterize phenomena, thus providing accurate answers to the questions being asked.

C.W. Emerson is with the Department of Geography, Geology, and Planning, Southwest Missouri State University, Springfield, MO 65804. (cwe836f@mail.smsu.edu).

N.S.N. Lam is with the Department of Geography and Anthropology, Louisiana State University, Baton Rouge, LA 70803.

D.A. Quattrochi is with the National Aeronautics and Space Administration, Global Hydrology and Climate Center, HR20, George C. Marshall Space Flight Center, Marshall Space Flight Center, AL 35812.

Generalization

Maps and other models of physical phenomena are simplified abstractions of reality and necessarily involve some degree of generalization. When performed correctly, generalization both reduces the volume of data that must be stored and analyzed and clarifies the analysis itself by separating signal from noise. For geographical analyses, a key concept in the generalization process is *scale* (Quatttochi, 1993). Cao and Lam (1997) outline various measures of scale:

- Cartographic scale — proportion of distance on a map to the corresponding distance on the ground
- Geographic (observational) scale — size or spatial extent of the study
- Operational scale — the spatial domain over which certain processes operate in the environment
- Measurement (resolution) scale — the smallest distinguishable object or parts of an object

Landscape processes are generally hierarchical in pattern and structure, and the study of the relation between the patterns at different levels in this hierarchy may provide a better understanding of the scale and resolution problem (Batty and Xie, 1996; Cao and Lam, 1997). Thus, an analyst must first understand the research question and the spatial domain of the process being measured (including the spatial organization of the features of interest) in order to determine the extent of the required input data and the cartographic scale of the output maps. The research question and the supporting inputs and outputs necessary to address the question, together with the availability of data and the capabilities of the analyst (knowledge, hardware, and software), then determine what resolution is needed in the input data.

Fractals

Quantifying the complex interrelation between these notions of size, generalization, and precision has proven to be a difficult task, although several measures such as univariate and multivariate statistics, spatial autocorrelation indices such as Moran's I or Geary's C, and local variance within a moving window (Woodcock and Strahler, 1987) provide some understanding of these interactions under given assumptions and within limits of certainty. An important area of research on this topic employs the concept of fractals (Mandelbrot, 1983) to determine the response of measures to scale and resolution (Goodchild and Mark, 1987; Goodchild and Klinkenberg, 1993; Lam and Quattrochi, 1992; Mark and Aronson, 1984). Fractals embody the concept of self-similarity, in which the spatial behavior or appearance of a system is largely independent of scale (Burrough, 1993). Self-similarity is defined

Photogrammetric Engineering & Remote Sensing, Vol. 65, No. 1, January 1999, pp. 51–61.

0099-1112/99/6501–0051$3.00/0

as a property of curves or surfaces where each part is indistinguishable from the whole, or where the form of the curve or surface is invariant with respect to scale. It is impossible to determine the size of a self-similar feature from its form; thus, photographs of geological strata usually include some object of known size for reference. An ideal fractal (or monofractal) curve or surface has a constant dimension over all scales (Goodchild, 1980), although it may not be an integer value. This is in contrast to Euclidean or topological dimensions, where discrete one, two, and three dimensions describe curves, planes, and volumes, respectively.

Theoretically, if the digital numbers of a remotely sensed image resemble an ideal fractal surface, then, due to the self-similarity property, the fractal dimension of the image will not vary with scale and resolution. However, most geographical phenomena are not strictly self-similar at all scales (Goodchild and Mark, 1987), but they can often be modeled by a stochastic fractal in which the scaling and self-similarity properties of the fractal have inexact patterns that can be described by statistics such as trail lengths, area-perimeter ratios, spatial autocovariances, and rank-order or frequency distributions (Burrough, 1993). Stochastic fractal sets relax the monofractal self-similiarity assumption and measure many scales and resolutions in order to represent the varying form of a phenomenon as a function of local variables across space (De Cola, 1993).

Multifractal fields are those in which the scaling properties of the field are characterized by a scaling exponent function. Rather than being described by a single fractal dimension, a multifractal field can be thought of as a hierarchy of sets corresponding to the regions exceeding fixed thresholds (De Cola, 1993). If $\varepsilon_\lambda(x)$ is a value in a multifractal field, then the probability of finding the a value of ε_λ greater than a given scale-dependent threshold λ is expressed as

$$\Pr(\varepsilon_\lambda > \lambda^\gamma) \approx \lambda^{-c(\gamma)} \quad (1)$$

where γ is the order of singularity (Pecknold *et al.*, 1997). λ is a resolution (as expressed as the square root of the ratio of the two-dimensional area to the areas of the smallest object represented in the image). $-c(\gamma)$ is the codimension function, which describes the sparseness of the field intensities. This equation describes how histograms of the density of interest vary with map resolution.

Pattern and Texture

In image interpretation, pattern is defined as the overall spatial form of related features, and the repetition of certain forms is a characteristic pattern found in many cultural objects and some natural features. Texture is the visual impression of coarseness or smoothness caused by the variability or uniformity of image tone or color (Avery and Berlin, 1992). A potential use of fractals concerns the analysis of image texture (De Cola, 1989; de Jong and Burrough, 1995). In these situations, it is commonly observed that the degree of roughness, or large brightness differences in short spatial intervals, in an image or surface is a function of scale and not of experimental technique. Very often, attempts to increase the precision of measurements by working at greater detail only result in the discovery of additional features that complicate analysis at the new scale (Burrough, 1993). The fractal dimension of remote sensing data could yield quantitative insight on the spatial complexity and information content contained within these data (Lam, 1990). Thus, remote sensing data acquired from different sensors and at differing spatial and spectral resolutions could be compared and evaluated based on fractal measurements (Jaggi *et al.*, 1993).

Texture can be measured using a variety of other indices such as variance, range, or standard deviation within a moving window. The differences in texture for images covering the same area but with different cartographic scales and resolutions can indicate the heterogeneity of the scene under observation. The higher the resulting textural parameter, the greater the degree of contrast or heterogeneity in the image. When texture analysis is applied to images of the same scene with different resolutions, the computed indices can be compared with regard to the changes that result from scaling. It is argued that the highest texture index indicates the highest variation and, thus, the resolution level at which most processes operate (Cao and Lam, 1997). The texture analysis method also operates on the assumption that the variability of the geographic data changes with scale and resolution, and the scale at which the maximum variability occurs is related to the operational domain of the processes depicted in the image. By finding the maximum variability of the data set, one could find the operational domain of the geographic phenomenon, thus aiding the selection of the appropriate resolution and spatial extent needed in the input imagery.

Overview of the Methodology

A software package known as the Image Characterization and Modeling System (ICAMS) (Quattrochi *et al.*, 1997) was used to explore:

- How changes in sensor spatial resolution affect the computed fractal dimension of ideal fractal sets,
- How fractal dimension is related to surface texture, and
- How changes in the relation between fractal dimension and resolution are related to differences in images collected at different dates.

ICAMS provides the ability to calculate the fractal dimension of remotely sensed images using the isarithm method (Lam and De Cola, 1993) (described below) as well as the variogram (Mark and Aronson, 1984) and triangular prism methods (Clarke, 1986). ICAMS also allows calculation of basic descriptive statistics, spatial statistics, and textural measures such as the local variance (Woodcock and Strahler, 1987), and contains utilities for aggregating images and generating specially characterized images, such as the Normalized Difference Vegetation Index (NDVI).

The ICAMS software was verified using simulated images of ideal fractal surfaces with specified dimensions. ICAMS was also used to analyze real imagery obtained by an aircraft-mounted high-resolution scanner and multi-date satellite imagery. The fractal dimension for areas of homogeneous land cover in the vicinity of Huntsville, Alabama was computed to investigate the relation between texture and resolution, and a multi-temporal analysis was carried out on Landsat Thematic Mapper images of the East Humboldt Range area in Nevada. Normalized Difference Vegetation Index (NDVI) images were used in each case, because ICAMS requires an eight-bit, single function data set, and because NDVI can readily be interpreted in terms of the urban/rural/forest contrasts in the Huntsville area and the in terms of the seasonal changes in vegetation pattern in the Nevada images.

Isarithm Method

The isarithm or line-divider method for calculating fractal dimension was used in this analysis due to its robustness, its accuracy, and its relative lack of sensitivity to input parameters. In this method, the fractal dimension of a curve (in a two-dimensional case) is measured using different step sizes that represent the segments necessary to traverse a curve (Lam and De Cola, 1993). For an irregular curve, as the step sizes become smaller, the complexity and length of the stepped representation of the curve increases. The fractal dimension D is derived from the equation

$$D = \log N / \log (1/G) \quad (2)$$

where G is the step size and N is the number of steps re-

quired to traverse the curve. If we plot the logarithm of the number of segments needed to traverse a curve for a range of step sizes versus the length of the curve and perform a linear regression, we get

$$\log L = C + \beta \log G \tag{3}$$

$$D = 1 - \beta \tag{4}$$

where L is the length of the curve, β is the slope of the regression of log (number of grid cell edges) versus log (step sizes), and C is a constant.

For surface representations (such as remotely sensed images), the isarithm method uses contours of equal z values as the objects of measurement whose fractal dimensions are estimated. The contours, or isarithms, are generated by dividing the range of pixel values into a number of equally spaced intervals. For each resulting isarithm line, the image is divided into two regions — areas above and below the isarithmic value. Each isarithm's length (as represented by the number of edges in a grid representation of a surface) is then measured at integer step sizes up to a user specified maximum. The logarithm of the number of edges is regressed against the log of the step sizes, producing a fractal plot. The slope of the regressed fractal plot is used to calculate the fractal dimension using Equation 4, resulting in a unique value of D for each isarithm. The fractal dimension of the entire image is calculated by averaging the computed fractal dimensions of only those isarithms that have fractal plots with $R^2 > 0.90$ (Jaggi *et al.*, 1993).

ICAMS also contains modules for analyzing the spatial autocorrelation of images. Moran's I and Geary's C (Cliff and Ord, 1973) are two indices of spatial autocorrelation which reflect the differing spatial structures of the smooth and rough surfaces. Moran's I is calculated from the following formula:

$$\mathrm{I}(d) = \frac{n \sum_i^n \sum_j^n w_{ij} z_i z_j}{W \sum_i^n z_i^2} \tag{5}$$

where w_{ij} is the weight at distance d so that $w_{ij} = 1$ if point j is within distance d from point i; otherwise, $w_{ij} = 0$; z's are deviations (i.e., $z_i = y_i - y_{\text{mean}}$ for variable y), and W is the sum of all the weights where $i \neq j$. Moran's I varies from +1.0 for perfect positive correlation (a clumped pattern) to −1.0 for perfect negative correlation (a checkerboard pattern).

Geary's C contiguity ratio, another index of spatial autocorrelation, is similar to Moran's I but uses the formula

$$\mathrm{C}(d) = \frac{(n-1) \sum_i^n \sum_j^n w_{ij} (y_i - y_j)^2}{2W \sum_i^n z_i^2} \tag{6}$$

with the same terms listed above. Geary's C normally ranges from 0.0 to 3.0, with 0.0 indicating positive correlation, 1.0 indicating no correlation, and values greater than 1.0 indicating negative correlation.

Moran's I and Geary's C differ from the fractal dimension in that D is focused on object shape, size, and the tortuosity of the edges of these objects. Moran's I and Geary's C are similar to join count statistics, but they operate on interval or ratio scale data. These measures do not explicitly consider the shapes and sizes of objects once the weights w_{ij} in Equations 5 and 6 are determined. This "topological invariance" (Cliff and Ord, 1973) shifts the focus in I and C to relative location, expressed as contiguity.

Fractional Brownian Surface Simulation

Ideal fractal surfaces having known dimensions were generated using the shear displacement method (Goodchild, 1980; Goodchild, 1982), as implemented in FORTRAN code provided by Lam and De Cola (1993). This method takes a grid matrix, initializes it to a uniform $z = 0$, and generates a succession of random lines across the grid surface. Along each line, the surface is faulted vertically to form a cliff. This process is repeated until several random fault lines are created between adjacent sample points. The intersections of these lines follow a Poisson distribution, while the angles of intersection are distributed uniformly between 0 and 2π. Each cliff's height is controlled by the user-specified parameter H, so that the variance between two points is proportional to their distance, as expressed in the variogram expression

$$\gamma(d) = \mathrm{E}[z(\mathbf{u}) - z(\mathbf{u} + h)]^2 \tag{7}$$

where $z(\mathbf{u})$ and $z(\mathbf{u} + h)$ are the z-values of a continuous surface at (x,y) locations represented by a vector $\mathbf{u}$, and h is the Euclidean distance, or lag between the points.

The class of variograms $\gamma(h) = h^{2H}$ are termed "fractional Brownian" (Goodchild, 1980) and have contours such that the fractal dimension D of the surface is equal to $3 - H$. The parameter H, which has values ranging from 0 to 1, describes the persistence of the surface — for large H, the surface has a strong tendency to return to neighboring values, and differences between adjacent points are small. For small H, the surface is highly irregular. An H value of 0.5 results in a Brownian surface that is statistically self-similar, so that if the intervals are rescaled by the ratio r^H, the rescaled surface has a probability distribution that is identical to the original (Burrough, 1993).

Figure 1 shows the effect of the H parameter. The surface with $H = 0.1$ is quite rough, with bright and dark pixels occurring at closely spaced intervals. Increasing H to 0.3 and 0.5 results in progressively smoother, more uniform surfaces. A surface with $H = 0.7$ bears a close resemblance to a topographical surface in the absence of any geomorphologic processes such as erosion that are not scale invariant. Goodchild and Mark (1987) have therefore proposed the use of artificially generated fractional Brownian surfaces as null hypotheses in geomorphologic studies.

The SURF_GEN program (Lam and De Cola, 1993) requires the user to input the number of rows and columns of the desired surface, the number of random cuts or cliffs in the surface, an H value, and a seed value for the random number generator. For this analysis, 1024- by 1024-pixel surfaces with $H = 0.1$, 0.3, 0.5, and 0.7 were generated using 5000 cuts and identical seed values. The resulting text files were converted to 8-bit images normalized to DN = 0 to 255.

An image pyramid approach (De Cola, 1993; De Cola, 1997) using simple averaging was used to generate coarser resolution images from the 1024 by 1024 originals. Suppose L is a positive integer with $n = 2^L$ and let X_0 be an n by n array of z values. By taking the mean of each 2^l by 2^l, $l = 0$, ..., L non-overlapping window in the original image (in this case the 1024 by 1024 output from SURF_GEN), one can generate a stack of $L + 1$ layers. While the size of the original $l = 0$ layer is $(2^L)^2$, the size of the complete image pyramid is only $4/3\ (2^L)^2$. Although the size of each layer is one-quarter that of the one below it, the amount of information declines more slowly than this (De Cola, 1993; De Cola, 1997).

As others (Woodcock and Strahler, 1987) have noted for the case of remotely sensed data, this simple averaging within a 2^l by 2^l window implies a square wave response on the part of the sensor. Although this is an oversimplification of actual sensor integration of reflectances within the instantaneous field of view, the simple averaging approach is sufficient to study the basic properties of statistical self-similarity in simulated and real world images. In the analysis of the

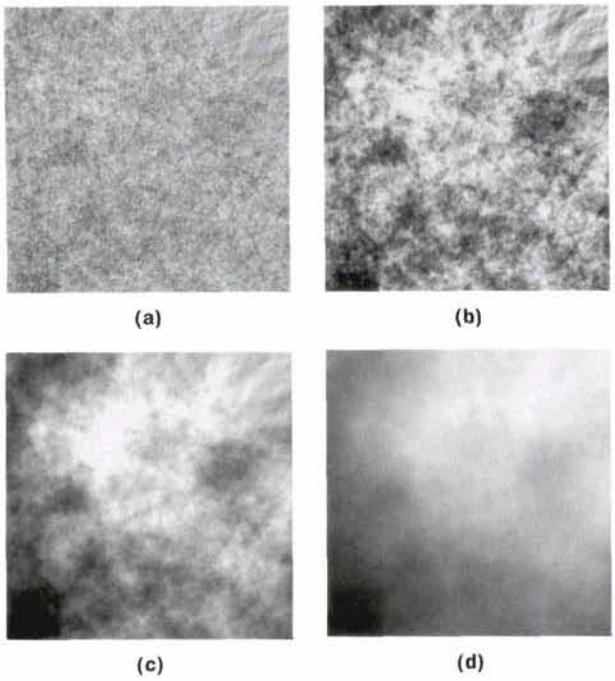

Figure 1. Simulated ideal fractal surfaces. 1024- by 1024-pixel images generated by the shear displacement method with the same random number seed. (a) $H = 0.1$, $D = 2.9$. (b) $H = 0.1$, $D = 2.9$. (c) $H = 0.1$, $D = 2.9$. (d) $H = 0.1$, $D = 2.9$.

simulated fractal surfaces $L = 10$, thus generating square surfaces with 1024, 512, 256, 128, and 64 pixels on a side. Surfaces smaller than 64 by 64 were not used in this analysis due to the limitations of the isarithm method, which requires a 48- by 48-pixel minimum surface for computing D with a step size of five.

Results of Fractional Brownian Surface Analysis

Because the maximum step size in the isarithm method is limited by the size of the image, D was computed for both the maximum possible number of steps for each averaged image and for five steps, the maximum number available for the smallest image size. The maximum number of steps allowed was nine steps for the 1024 by 1024 image. Table 1 lists the descriptive statistics for the ideal fractal surfaces. Table 1 shows that the mean and median digital numbers for each H value remain approximately the same when the pixels are aggregated into larger cells. Standard deviation of the digital numbers (DN) decreases drastically with increasing aggregation for the $H = 0.1$ surface, but changes very little for the $H = 0.7$ surface. Adjacent cells have similar values in the smoother surfaces with high H (and low fractal dimension), while averaging groups of adjacent cells has a more pronounced smoothing effect on the irregular surface.

Figure 2 shows D for each of the four fractional Brownian surfaces generated with the SURF_GEN program. The fractal dimensions estimated by ICAMS generally agree with the known dimensions of each surface, although there is a tendency for the isarithm method to overestimate, particularly at lower values of H (and consequently higher fractal dimensions). Specifying five as the maximum possible number of steps made little difference in the estimated dimension, although using the maximum possible number of steps increased the overestimation at lower H values. The fairly linear response across resolutions is a characteristic of ideal fractal surfaces and demonstrates the concept of self-similarity — for these monofractal surfaces, the complexity of the image remains the same across scales.

Table 2 lists the error (difference between computed D and the $D = 3 - H$ that was specified in the SURF_GEN program) for each resolution and H-value along with the overall root-mean-squared error (RMSE, square root of the mean of the squared differences between the estimated D and the D resulting from the specified H value). The least bias and lowest standard deviation occur at $H = 0.5$ for both the maximum number of steps and a fixed step size of five. In general, a fixed step size generated the least RMSE across all values of H, although the lowest error was obtained at $H = 0.5$ for the maximum number of steps.

The ICAMS local variance utility was used to compute the variance of pixels within a moving 3 by 3 window. This utility generates a texture map of the image and computes the global mean standard deviation of the DNs in the moving window. Figure 3 shows the effect of pixel aggregation and scaling on the mean standard deviation (MSD) within the 3

TABLE 1. STATISTICS OF IDEAL FRACTAL SURFACES

H	Pixel Size	Image Size	Max Steps	D Max Step	R^2 Max Step	D 5 Step	R^2 5 Step	Mean DN	Median DN	DN Std. Dev.	Moran's I	Geary's C	Mean Std. Dev
0.1	1	1024 × 1024	9	3.0193	0.9990	2.9830	0.9917	127.50	128	42.26	0.1878	0.8122	35.09
0.1	2	512 × 512	8	3.0431	0.9959	2.9658	0.9950	127.63	128	25.71	0.2874	0.7127	22.67
0.1	4	256 × 256	7	2.9988	0.9852	2.9914	0.9922	127.53	128	17.27	0.4206	0.5793	21.49
0.1	8	128 × 128	6	3.0219	0.9908	2.9972	0.9879	127.52	128	12.77	0.4907	0.5091	33.20
0.1	16	64 × 64	5	3.0362	0.9805	3.0362	0.9805	127.50	128	9.88	0.4925	0.5081	62.97
0.3	1	1024 × 1024	9	2.8901	0.9926	2.8052	0.9990	127.58	129	42.15	0.8614	0.1386	17.52
0.3	2	512 × 512	8	2.8391	0.9892	2.7488	0.9948	127.71	129	39.73	0.8995	0.1005	16.88
0.3	4	256 × 256	7	2.8134	0.9854	2.7258	0.9910	127.61	129	38.02	0.8967	0.1033	21.33
0.3	8	128 × 128	6	2.7728	0.9860	2.7398	0.9866	127.59	129	36.30	0.8727	0.1274	34.35
0.3	16	64 × 64	5	2.7509	0.9841	2.7509	0.9841	127.58	129	34.31	0.8304	0.1699	63.98
0.5	1	1024 × 1024	9	2.5294	0.9869	2.4954	0.9882	127.76	132	41.62	0.9972	0.0028	10.63
0.5	2	512 × 512	8	2.4923	0.9846	2.4454	0.9899	127.88	132	41.58	0.9964	0.0036	12.57
0.5	4	256 × 256	7	2.4816	0.9807	2.4430	0.9823	127.79	132	41.51	0.9935	0.0065	18.41
0.5	8	128 × 128	6	2.4692	0.9779	2.4597	0.9787	127.77	132	41.38	0.9871	0.0129	32.53
0.5	16	64 × 64	5	2.4753	0.9725	2.4753	0.9725	127.76	132	41.14	0.9737	0.0263	62.98
0.7	1	1024 × 1024	9	2.1489	0.9702	2.1631	0.9871	127.54	137	42.37	0.9999	0.0001	8.60
0.7	2	512 × 512	8	2.1281	0.9702	2.1212	0.9845	127.63	137	42.36	0.9999	0.0001	11.79
0.7	4	256 × 256	7	2.1288	0.9645	2.1250	0.9744	127.57	137	42.36	0.9997	0.0003	17.97
0.7	8	128 × 128	6	2.1406	0.9671	2.1269	0.9608	127.55	137	42.36	0.9993	0.0008	32.22
0.7	16	64 × 64	5	2.1443	0.9652	2.1279	0.9602	127.55	137	42.34	0.9978	0.0026	62.71

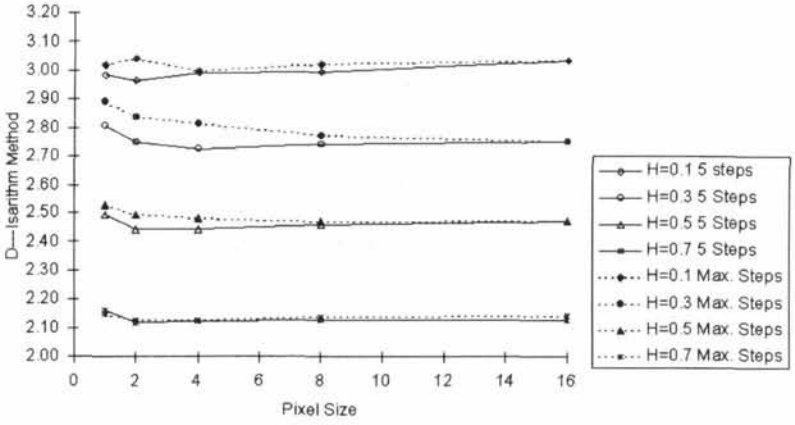

Figure 2. Ideal fractal surface dimension.

TABLE 2. DEVIATIONS FROM KNOWN FRACTAL DIMENSION — ISARITHM METHOD

	Five Steps				Maximum Possible Steps			
Pixel Size	$H = 0.1$	$H = 0.3$	$H = 0.5$	$H = 0.7$	$H = 0.1$	$H = 0.3$	$H = 0.5$	$H = 0.7$
1	0.0830	0.1052	−0.0046	−0.1369	0.1193	0.1901	0.0294	−0.1511
2	0.0658	0.0488	−0.0546	−0.1788	0.1431	0.1391	−0.0077	−0.1719
4	0.0914	0.0258	−0.0570	−0.1750	0.0988	0.1134	−0.0184	−0.1712
8	0.0972	0.0398	−0.0403	−0.1731	0.1219	0.0728	−0.0308	−0.1594
16	0.1362	0.0509	−0.0247	−0.1721	0.1362	0.0509	−0.0247	−0.1557
RMSE	0.0975	0.0605	0.0412	0.1679	0.1248	0.1235	0.0238	0.1621

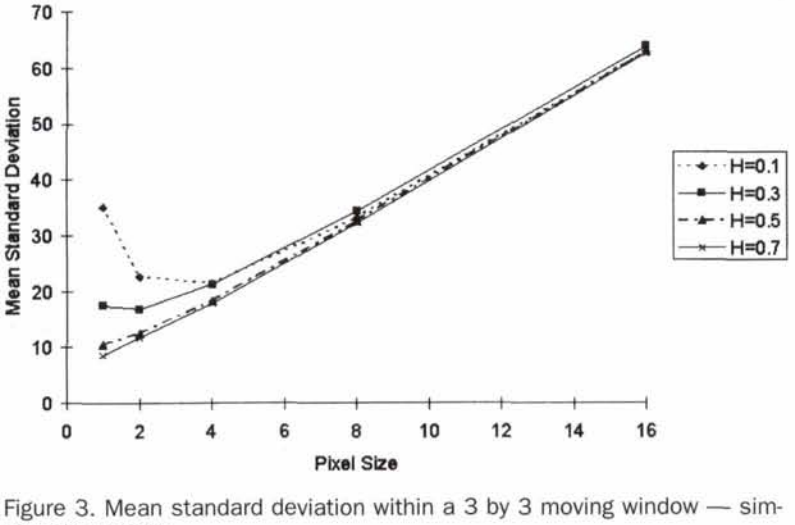

Figure 3. Mean standard deviation within a 3 by 3 moving window — simulated surfaces.

by 3 moving window. The MSD initially decreases with aggregation, more rapidly for the $H = 0.1$ image, less so for the smoother images. After the first aggregation step, the fixed 3 by 3 window size encompasses larger and larger areas of the original ungeneralized surface (albeit with only nine pixels) and this factor leads to a trend of increasing MSD for all of the artificial surfaces, because progressively larger portions of the original 1024 by 1024 surface are incorportated into nine generalized pixels. Scaling the moving window size to correspond to the generalized pixels at each step of aggregation was not possible due to the 10 by 10 maximum limit imposed by the ICAMS local variance utility.

Huntsville Texture Analysis

High resolution imagery of the Huntsville, Alabama area was used to evaluate the differences in fractal dimension that occur among textures associated with differing land covers. Huntsville (Figure 4) is a medium-sized city located at the southern end of the Appalachian Mountains in northern Alabama. Mission M424 conducted by the Lockheed Engineering and Science Company collected 5- and 10-meter resolution data using the Advanced Thermal and Land Applications (ATLAS) sensor system mounted in a NASA Learjet. The collection date was 7 September 1994, a clear day with less

than 5 percent cloud cover. ATLAS is a 15-channel imaging system that incorporates the bandwidths of the Landsat Thematic Mapper with additional bands in the middle reflective infrared and thermal infrared range (Table 3). The daytime data were collected around local solar noon and then repeated two to three hours after sunset. Beginning at 1100 local time, nine daytime flight lines were flown from an altitude of 5000 meters to image at 10 meters resolution, and six flight lines were flown at an altitude of 2500 meters to image at 5 meters resolution. All flight lines were repeated at night beginning at 2030 local time. Color infrared photography was also acquired during the daytime flights (f = 152 mm, 23- by 23-cm format). Ground data collection, including the establishment of GPS control points, measurement of surface temperatures at selected sites representing different cover types, and concurrent launches of radiosondes were also carried out during the overflights (Lo *et al.*, 1997). The 10-meter data were registered to a digital line graph model of the Huntsville area that had been updated to include GPS horizontal control points.

384- by 384-pixel images containing homogeneous land uses were obtained from the 10-meter ATLAS data set (Figures 4 and 5). Three land uses were analyzed: (1) an agricultural area located north of Huntsville, (2) a forested area located in the mountains to the southeast of town, and (3) an urban area containing the central business district and adjacent commercial/residential areas. The agricultural area contains large cotton fields and pastures devoted to grazing, with a sparse road network oriented generally along the cardinal directions. The image of the forested area is fairly uniform, because the 10-meter resolution is insufficient to resolve individual trees. Topographical features such as the valley extending from the northwest corner to the south central part of the image are the main distinguishing features. The urban image is highly complex, with individual streets and buildings clearly visible. Large commercial buildings associated with the central business district are visible in the southeast part of the image, and shopping centers extend along U.S. Highway 431 from the south to northeast.

TABLE 3. ATLAS CHANNELS

Channel #	Bandwidth (μm)
1	0.45–0.52
2	0.52–0.60
3	0.60–0.63
4	0.63–0.69
5	0.69–0.76
6	0.76–0.90
7	1.55–1.75
8	2.08–2.35
9	3.35–4.20
10	8.20–8.60
11	8.60–9.00
12	9.00–9.40
13	9.60–10.2
14	10.2–11.2
15	11.2–12.2

In an earlier analysis of the Huntsville ATLAS data, Lo *et al.* (1997) found significant correlations between the day and night time irradiances of various types of land covers and images of the Normalized Difference Vegetation Index (NDVI). NDVI showed a very strong negative correlation with the irradiance of residential, agricultural, and vacant land uses, implying that vegetation tends to bring down the surface temperatures, especially during the daytime. In the analysis presented here, NDVI was computed for the agricultural, forest, and urban images at a 10-meter resolution (384 by 384 pixels) and for coarser resolution images having 20-, 40-, and 80-m square pixels using an image pyramid approach (De Cola, 1993; De Cola, 1997) using the mean of 4-, 16-, and 64-pixel composites of the original 10-m square pixels. NDVI was computed from the ATLAS channel 6 (near infrared) and 4 (red) images using the following formula:

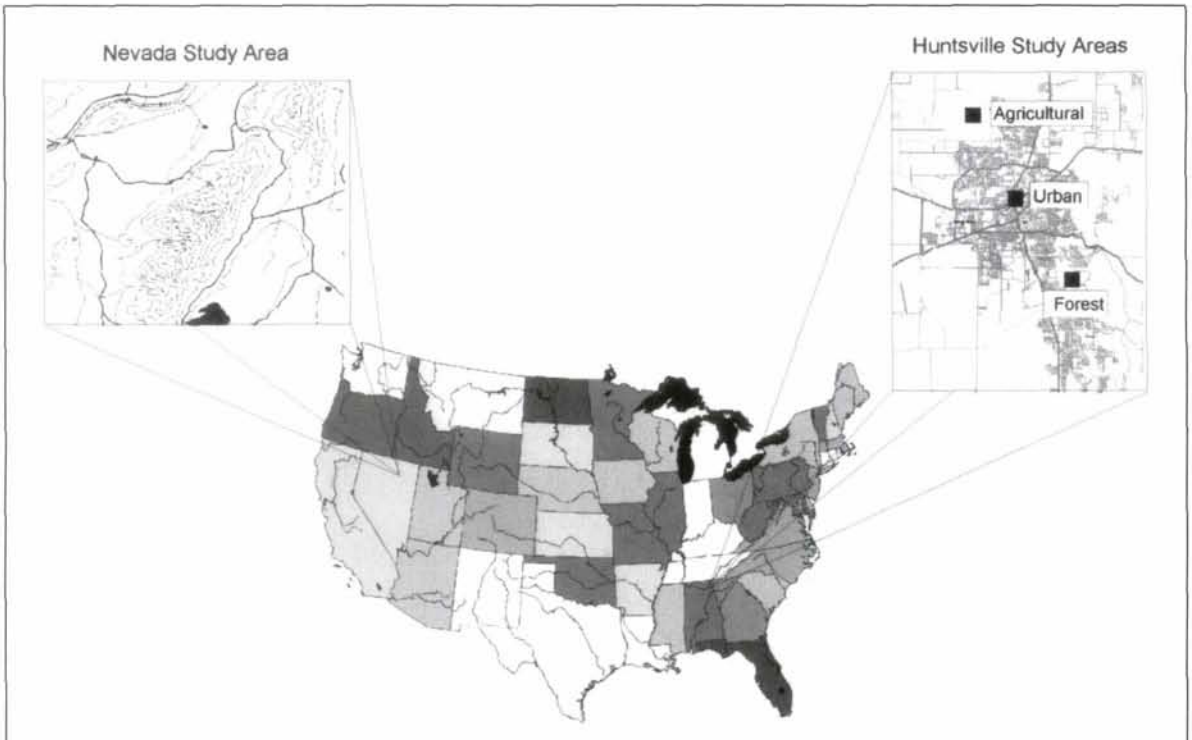

Figure 4. Location of Nevada and Huntsville study areas.

$$\text{NDVI} = (\text{ch6} - \text{ch4})/(\text{ch6} + \text{ch4}). \quad (8)$$

NDVI varies from −1 to +1, and provides a good indication of the amount of photosynthetically active biomass in the image. Snow, water, clouds, moist soil, and highly reflective non-vegetated surfaces generally have NDVI values less than zero, rock and dry soils have values close to zero, and highly vegetated surfaces have indices close to +1.0. NDVI varies across spatial extents in a complex fashion due to influences of the varying domains of topography, slope, availability of solar radiation, and other factors (Walsh *et al.*, 1997).

The ICAMS isarithm method with step size of five and contour interval of ten was used to compute fractal dimension for the three land uses. The ICAMS software computed very high fractal dimensions (in some cases exceeding the theoretical limit of $D = 3.0$) for images of the raw floating point NDVI values. Rescaling the NDVI values to an 8-bit format facilitated comparisons between the three land-cover textures and helped illustrate how changes in resolution affect the computed fractal dimension. Table 4 shows the descriptive statistics for the 10-meter image and the coarser resolution surfaces with 20-, 40-, and 80-meter square pixels. The image size and the range of resolutions was limited at the upper end by the need to get a homogeneous land cover (thus limiting the maximum size of the image) and at the lower end by the minimum image size (48 by 48 pixels) necessary to use five steps in the isarithm method of computing fractal dimension. The ATLAS 5-meter data were not used because sufficiently large forested and agricultural areas were not imaged in the six flight lines obtained at the lower altitude.

Decreasing resolution affected the non-spatial variance of the three land covers in different ways. Variance dropped by a moderate amount for the agricultural image and by a greater amount in the forested image, but it changed very little for the urban image. Moran's I dropped as resolution decreased from 10- to 80-meter pixels in the agricultural and urban images (indicating decreasing spatial autocorrelation), and the spatial statistics increased then declined in the forested image. The mean standard deviation within a 3 by 3 moving window for all three land covers increased with decreasing resolution as the larger pixels encompassed larger areas of the ground surface. These measures provide indications that convolving groups of small pixels into larger pixels by taking the mean DN (and by extension, imaging at different resolutions) affects both the non-spatial distribution of the values in an image as well as the relation between features in the image.

Unlike the ideal fractal surfaces, real world images are rarely self-similar, so one would expect fractal dimension to vary with the resolution of the sensor. Figure 6 shows that over the 10- to 80-meter range of resolutions, the agricultural image D increases from just over 2.6 to more than 2.9. The forest image shows a general decline in D with decreasing

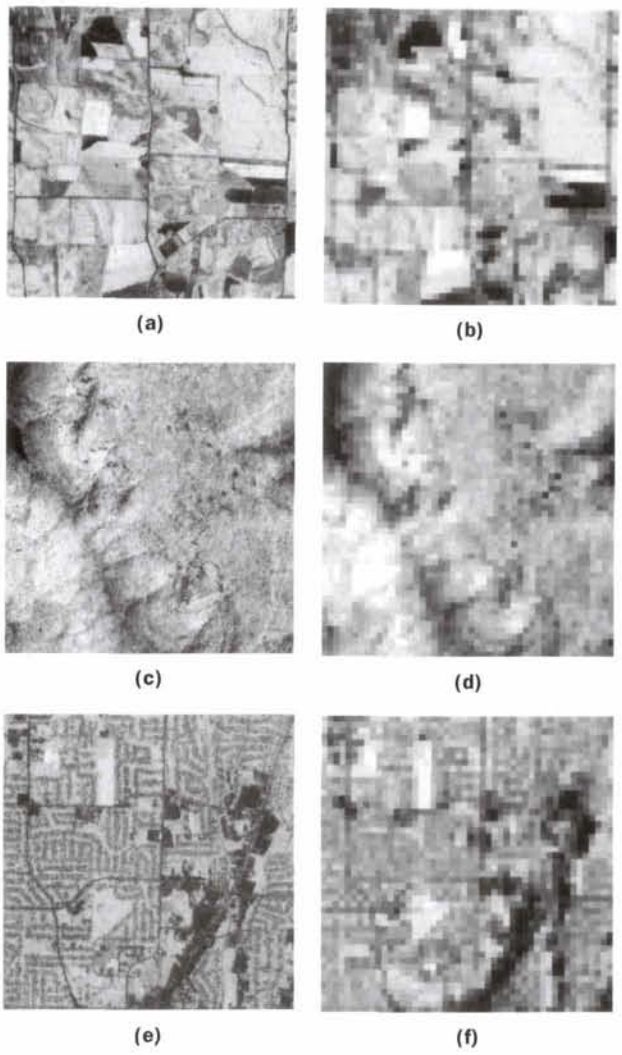

Figure 5. ATLAS NDVI images of the Huntsville, Alabama region. (a) Agricultural area, 10-m resolution. (b) Agricultural area, 80-m resolution. (c) Forested area, 10-m resolution. (d) Forested area, 80-m resolution. (e) Urban area, 10-m resolution. (f) Urban area, 80-m resolution.

TABLE 4. DESCRIPTIVE STATISTICS — HUNTSVILLE NDVI TEXTURE ANALYSIS

Land Cover	Pixel Size (m)	Image Size	D	Mean R^2	Mean DN	Median DN	DN Std. Dev.	Moran's I	Geary's C	Mean Std. Dev
Ag.	10	384 × 384	2.6101	0.9904	127.10	137	42.18	0.9023	0.0978	19.92
	20	192 × 192	2.6640	0.9817	127.13	137	42.10	0.8763	0.1237	30.00
	40	96 × 96	2.7893	0.9680	127.15	136	41.97	0.8217	0.1773	53.26
	80	48 × 48	2.9371	0.9754	127.22	134.5	41.79	0.7369	0.2612	102.76
Forest	10	384 × 384	2.8667	0.9920	127.73	132	38.68	0.7557	0.2443	23.35
	20	192 × 192	2.8229	0.9900	127.86	132	38.19	0.7830	0.2171	30.94
	40	96 × 96	2.8159	0.9933	127.89	131	37.73	0.8073	0.1937	52.67
	80	48 × 48	2.7419	0.9754	128.02	131	37.53	0.7932	0.2105	101.93
Urban	10	384 × 384	2.7417	0.9903	127.01	137	42.50	0.7587	0.2413	24.96
	20	192 × 192	2.7471	0.9924	127.00	133	42.50	0.7595	0.2407	32.88
	40	96 × 96	2.7734	0.9798	126.99	132	42.50	0.7063	0.2947	54.95
	80	48 × 48	2.7829	0.9763	127.00	133	42.51	0.6726	0.3301	103.32

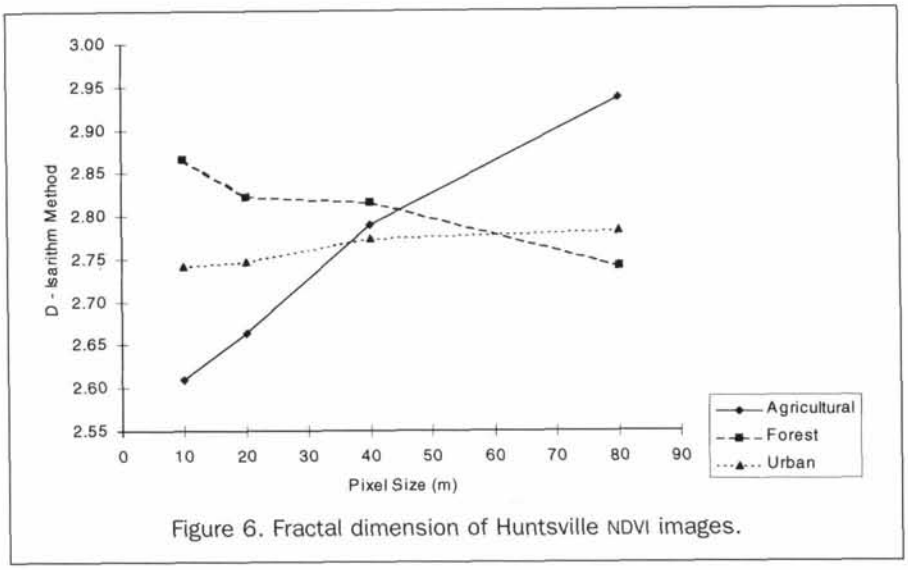

Figure 6. Fractal dimension of Huntsville NDVI images.

resolution, and averaging the original 10-meter pixels into larger pixels has only a small negative effect on the computed D value, as indicated by the negative 95 percent confidence interval for the slope of the regression for the forest data (Table 5).

The forested scene behaves as one would expect — larger pixel sizes decrease the complexity of the image as individual clumps of trees are averaged into larger blocks. It is likely that the tortuosity of isarithms of gray values in the forested image (as indicated by a higher D value) would be greater if the sensor were able to resolve individual trees within the scene. The urban image behaves most like an ideal fractal surface and can be said to be self-similar over the range of pixel sizes analyzed, because one cannot reject the hypothesis that the slope of the pixel size-fractal dimension relation is equal to zero. The 95 percent confidence interval for the regression slope overlaps zero (although just barely at the low end). The slope of the changes in D with changes in resolution for the three land uses indicates how agricultural, urban, and forested areas compare over the range of pixel sizes considered. It should be noted, however, that these regressions are based on only one image and four pixel sizes in a limited range for each land-cover type. Although the R^2 values for the agriculture and forest images is 0.94 or higher, the regression of the urban resolution-D relation, 0.87 is not as strongly linear.

The increased complexity of the agricultural image with increasing pixel size results from the loss of homogeneous groups of pixels in the large fields to mixed pixels composed of varying combinations of NDVI values that correspond to roads and vegetation. Figure 5 shows that, as resolution decreases in the agricultural image, the roads tend to appear wider and the fields are smaller, until eventually the image appears very complex, with few homogeneous areas. This is also reflected in the changes in Moran's I statistic in Table 4. The I statistic for the agricultural area drops from approximately 1.0 (indicating a high level of spatial autocorrelation) to 0.74, indicating a more dispersed spatial arrangement of values in the image as resolution grows more coarse. The same process occurs in the urban image to some extent, but the lack of large, homogeneous areas in the high resolution NDVI image means the initially high D value is maintained as pixel size increases.

East Humboldt Range, Nevada

Texture is not the only factor used in differentiating between different land covers — shape, size, pattern, shadow, tone, and association are others (Avery and Berlin, 1992). Although this paper does not directly analyze the effects of object shape on computed fractal dimension, it does examine a large complex scene in a multi-temporal context to analyze the effects on D. This investigation used Landsat Thematic Mapper images of the East Humboldt Range area of northern Nevada that were obtained as part of a long-term field study conducted from May 1993 through October 1994 (Laymon *et al.*, 1998).

This area of the Great Basin (Figure 4) contains several parallel ranges of roughly 3000-m mountains separated by broad valleys at about 1800 m above sea level. The mountain ranges in this region have sparse vegetation and thin soil with low infiltration capacities. Much of the existing vegetation occurs in desert valleys or on alluvial fans adjacent to the mountains. Vegetative growth is most abundant where subsurface water flows close enough to the surface to be accessible to plants. The valley is dominated by shrub vegetation with understory forbs and grasses. Sagebrush is common

TABLE 5. REGRESSION OF HUNTSVILLE NDVI FRACTAL DIMENSION VERSUS PIXEL SIZE

Land Cover	Parameter	Coefficients	Std. Err.	R^2	t	P	Lower 95.0%	Upper 95.0%
Agriculture	Intercept	2.5753	0.0196		131.2215	0.0001	2.4909	2.6598
	Resolution	0.0047	0.0004	0.9836	10.9495	0.0082	0.0028	0.0065
Forest	Intercept	2.8727	0.0132		217.4644	0.0000	2.8159	2.9295
	Resolution	−0.0016	0.0003	0.9413	−5.6617	0.0298	−0.0029	−0.0004
Urban	Intercept	2.7386	0.0075		366.8163	0.0000	2.7065	2.7708
	Resolution	0.0006	0.0002	0.8742	3.7277	0.0650	−0.0001	0.0013

on the higher elevations of the well-drained alluvial fans, and it eventually gives way to grasses, forbs, and small perennials at lower elevations (Laymon *et al.*, 1998).

Figure 7 shows Landsat Thematic Mapper NDVI images of the East Humboldt Range that were obtained in May and August, 1993. The Humboldt Range area was imaged during the peak "green up" period in early summer of 1993 and "dry down" in late summer 1993. The imagery was obtained from EOSAT Corp. and was system-corrected, orbit-oriented (type P data) that was made available at no cost to the investigators through an agreement between EOSAT and NASA on behalf of the U.S. Global Change Research Program. System-corrected data are geometrically adjusted for the spacecraft's orientation and predicted position. The images show the Ruby Mountains in the south and the East Humboldt Range in the north. Drainage extends from the mountains westward through Lamoille Creek, which flows northward from the bottom part of the image through Lamoille Valley, and Secret Creek, which drains the narrow valley between the two mountain ranges. The Humboldt River flows northeastward through the upper left part of the image. Interstate 80 and a railroad operated by the Union Pacific follow the general course of the river. Nevada Highway 229 follows Secret Creek and joins I-80 northwest of Phyllis Lake. The East Humboldt Range has several channels draining eastward into Clover Valley in the upper right corner of the image.

As in the Huntsville example, rescaled 8-bit NDVI images were compared. Images of TM bands 4 and 3 were normalized to account for illumination differences between the two dates, and the pixels in each image were averaged to resolutions of 60, 120, 240, 480, and 960 meters from the original 30-meter pixel size. Table 6 shows the descriptive statistics for the original 30-meter data and the coarser-resolution NDVI images. The two images have similar means and standard deviations that do not change appreciably with decreasing resolution. As with the simulated surfaces and Huntsville ATLAS data sets, the mean standard deviation within a 3 by 3 moving window increased with decreasing resolution as the window encompassed larger and larger areas on the ground.

Figure 7 shows the NDVI values for May. This image shows large dark (low NDVI) areas in mountains corresponding to snow cover. Bright (high NDVI) areas are located along the middle slopes of the mountains, along stream beds, and in irrigated fields. The brightest areas in the August image are near the peaks of the mountains. Vegetation remained active at higher elevations, while the long summer drought caused vegetation at lower elevations to senesce, as indicated by the retreat of high NDVI values in the valleys.

The graph of the response of fractal dimension to rescaling (Figure 8) shows a much more complex pattern than ideal fractal surfaces or the homogeneous land-cover images of Huntsville. D is no longer independent of resolution, as in the ideal fractal surfaces and is not a linear function of resolution (except over subsets of the overall range of pixel sizes). The positive, fairly linear slope of the change in D for the August image shows an increase of complexity as pixel size increases up to 480 meters. The D values in the May image show a more complex relation to pixel size, with an initial rise in D followed by a short decline, then a long increase. This may be due to the influence of aggregating pixels on the boundaries of the large snow covered areas with high NDVI values on the adjacent mountain slopes. The resulting mixed pixels tend to blur the sharp distinction between snow and vegetative cover, thus altering the shapes and areas of homogeneous NDVI values for the snow cover and lower slopes. The fractal dimensions of an image created from the differences in the May and August NDVI values increase with pixel size up to a resolution of 120 meters, then

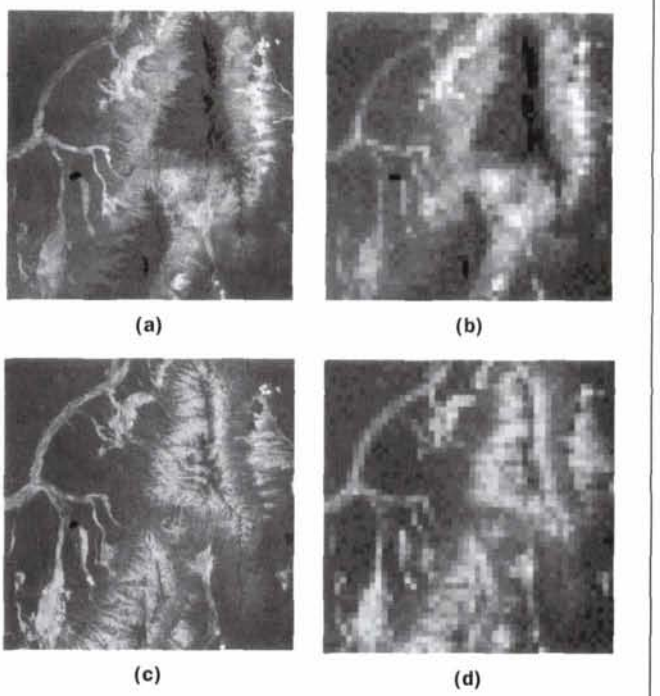

Figure 7. East Humboldt Range area, Nevada — NDVI images. (a) May 1993, 30-m resolution. (b) May 1993, 960-m resolution. (c) August 1993, 30-m resolution. (d) August 1993, 960-m resolution.

TABLE 6. DESCRIPTIVE STATISTICS — NDVI IMAGES, EAST HUMBOLDT RANGE, NEVADA

Date	Pixel Size (m)	Image Size	D	Mean R^2	Mean DN	Median DN	DN Std. Dev	Moran's I	Geary's C	Mean Std. Dev
May, 1993	30	1600 × 1600	2.6252	0.9895	127.03	114	41.73	0.9621	0.0379	12.61
	60	800 × 800	2.6646	0.9919	126.97	111	41.86	0.9484	0.0516	14.49
	120	400 × 400	2.6651	0.9932	126.94	114	41.91	0.9366	0.0634	18.68
	240	200 × 200	2.6347	0.9926	126.92	115	41.93	0.9200	0.0802	29.27
	480	100 × 100	2.7108	0.9654	126.94	115	42.03	0.8954	0.1048	53.37
	960	50 × 50	2.8026	0.9546	126.93	116	42.24	0.8540	0.1462	104.43
August, 1993	30	1600 × 1600	2.6040	0.9862	126.99	111	42.45	0.9673	0.0327	12.49
	60	800 × 800	2.6337	0.9908	126.99	111	42.46	0.9407	0.0593	15.10
	120	400 × 400	2.6490	0.9844	126.98	111	42.44	0.8155	0.0845	19.65
	240	200 × 200	2.6837	0.9886	126.98	112	42.46	0.8894	0.1107	30.12
	480	100 × 100	2.7632	0.9896	126.98	113	42.48	0.8558	0.1445	53.96
	960	50 × 50	2.6861	0.9923	127.00	117	42.52	0.8011	0.1991	104.81

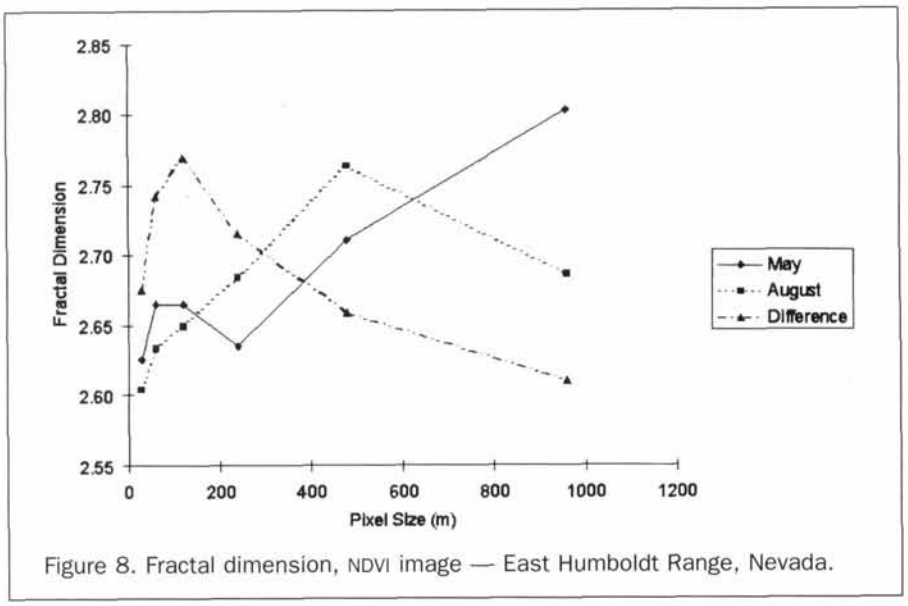

Figure 8. Fractal dimension, NDVI image — East Humboldt Range, Nevada.

decline with increasing pixel size. This means that the greatest complexity in the difference image occurs around resolutions of 120 meters, and this is analogous to the operational domain of changes in vegetation and snow cover that constitute differences in the two dates.

Conclusions

This investigation verified that the ICAMS isarithm method estimates the fractal dimensions of simulated monofractal surfaces generated by the SURF_GEN program most accurately at $H = 0.5$, with over- and underestimations at greater or lesser H values. The example surfaces exhibit relatively constant fractal dimensions with aggregation, thus indicating the self-similar nature of these ideal monofractal data sets.

The ICAMS software together with the data pyramid approach allow efficient exploration of scaling behavior, because the averaged images do not require more than four-thirds the original image storage capacity (De Cola, 1993; De Cola, 1997). This allows selection of an optimal resolution for characterizing geographical phenomena, such as the changes in vegetation and snow cover patterns. Operating on the assumption that the scale at which the highest fractal dimension is measured may be the scale at which most of the processes operate (Goodchild and Mark, 1987; Lam and Quattrochi, 1992), one can conclude that the differences in the NDVI images of the East Humbold Range, Nevada are due to processes that are best represented at a resolution of 120 meters.

In the Huntsville example presented here, the complexity of NDVI images of agriculture, forest, and urban areas responds differently to aggregation. The image of the agricultural area grew more complex as the pixel size was increased from 10 to 80 meters, while the forested area grew slightly smoother and the complexity of the urban area remained approximately the same. In examining the changes in fractal dimensions with changing pixel size in Figure 5, an obvious question to ask is whether it is best to use a fine resolution for analyzing complex scenes with heterogeneous land uses, or is it best to select a resolution where the complexity of each land cover is approximately the same (around 40 meters pixel size). If one is wishing to distinguish between the different land covers, then the resolution at which the greatest differences in complexity occurs is optimal. If the question is concerned with determining lumped characteristics of a heterogeneous scene, then the resolution with the least differences in fractal dimension will likely provide more unbiased estimates of the scene taken as a whole.

More research is needed to examine how the complexity of a geographical process having a known spatial operational scale is depicted in remotely sensed images. This process domain benchmark would allow significance testing of the fractal dimension's response to changes in resolution. Processes that are more scale independent (closer to the monofractal ideal) require fewer data (i.e., lower resolutions) than other processes that are highly scale dependent. For instance, relating NDVI values to irradiance (Lo *et al.*, 1997) or emissivity (Laymon *et al.*, 1998) would allow an analyst to make inferences as to how agriculture, forest cover, and urbanization (as measured in remotely sensed images) affects heat flux at regional scales. No one resolution is optimal for all of these, so further investigation is needed to determine how the fractal dimension can be used to provide indications of the tradeoffs involved in selecting the scale, resolution, and spatial extent of the input imagery.

Acknowledgments

This research was supported by a NASA-ASEE Summer Faculty Fellowship to C.W. Emerson and a NASA research grant to N.S.N Lam and D.A. Quattrochi (Award No. NAGW-4221).

References

Avery, T.E., and G.L. Berlin, 1992. *Fundamentals of Remote Sensing and Airphoto Interpretation*, Macmillan Publishing Co., New York, 472 p.

Batty, M., and Y. Xie, 1996. Preliminary Evidence for a Theory of the Fractal City, *Environment and Planning A*, 28(10):1745–1763.

Burrough, P.A., 1993. Fractals and Geostatistical Methods in Landscape Studies, *Fractals in Geography* (N.S.N. Lam and L. De Cola, editors), Prentice Hall, Englewood Cliffs, New Jersey, pp. 87–121.

Cao, C., and N.S.N. Lam, 1997. Understanding the Scale and Resolution Effects in Remote Sensing and GIS, *Scale in Remote Sensing and GIS* (D.A. Quattrochi and M.F. Goodchild, editors), CRC Press, Boca Raton, Florida, pp. 57–72.

Clarke, K.C., 1986. Computation of the Fractal Dimension of Topographic Surfaces Using the Triangular Prism Surface Area Method, *Computers and Geosciences*, 12(5):713–722.

Cliff, A.D., and J.K. Ord, 1973. *Spatial Autocorrelation*, Pion Limited, London, 178 p.

De Cola, L., 1989. Fractal Analysis of a Classified Landsat Scene, *Photogrammetric Engineering & Remote Sensing*, 55(5):601–610.

———, 1993. Multifractals in Image Processing and Process Imaging, *Fractals in Geography* (N.S.N. Lam and L. De Cola, editors), Prentice Hall, Englewood Cliffs, New Jersey, pp. 282–304.

———, 1997. Multiresolution Covariation among Landsat and AVHRR Vegetation Indices, *Scale in Remote Sensing and GIS* (D.A. Quattrochi and M.F. Goodchild, editors), CRC Press, Boca Raton, Florida, pp. 73–92.

de Jong, S.M., and P.A. Burrough, 1995. A Fractal Approach to the Classification of Mediterranean Vegetation Types in Remotely Sensed Data, *Photogrammetric Engineering & Remote Sensing*, 56(8):1041–1053.

Goodchild, M.F., 1980. Fractals and the Accuracy of Geographical Measures, *Mathematical Geology*, 12(2):85–98.

———, 1982. The Fractional Brownian Process as a Terrain Simulation Model, *Proceedings, 13th Annual Pittsburgh Conference on Modeling and Simulation*, pp. 1133–1137.

Goodchild, M.F., and B. Klinkenberg, 1993. Statistics of Channel Networks on Fractional Brownian Surfaces, *Fractals in Geography* (N.S.N. Lam and L. De Cola, editors), Prentice Hall, Englewood Cliffs, New Jersey, pp. 122–141.

Goodchild, M.F., and D.M. Mark, 1987. The Fractal Nature of Geographic Phenomena, *Annals of the Association of American Geographers*, 77(2):265–278.

Jaggi, S., D.A. Quattrochi, and N.S.N. Lam, 1993. Implementation and Operation of Three Fractal Measurement Algorithms for Analysis of Remote Sensing Data, *Computers and Geosciences*, 19(6):745–767.

Lam, N.S.N., 1990. Description and Measurement of Landsat TM Images Using Fractals, *Photogrammetric Engineering & Remote Sensing*, 56(2):187–195.

Lam, N.S.N., and L. De Cola, 1993. Fractal Simulation and Interpolation, *Fractals in Geography* (N.S.N. Lam and L. De Cola, editors), Prentice Hall, Englewood Cliffs, New Jersey, pp. 56–74.

Lam, N.S.N., and D.A. Quattrochi, 1992. On the Issues of Scale, Resolution, and Fractal Analysis in the Mapping Sciences, *Professional Geographer*, 44(1):88–97.

Laymon, C., D. Quattrochi, E. Malek, I. Hipps, J. Boettinger, and G. McCurdy, 1998. Remotely-Sensed Regional-Scale Evapotranspiration of a Semi-Arid Great Basin Desert and Its Relationship to Geomorphology, Soils, and Vegetation, *Geomorphology*, 21(3–4): 329–349.

Lo, C.P., D.A. Quattrochi, and J.C. Luvall, 1997. Application of High-Resolution Thermal Infrared Remote Sensing and GIS to Assess the Urban Heat Island Effect, *International Journal of Remote Sensing*, 18(2):287–304.

Mandelbrot, B.B., 1983. *The Fractal Geometry of Nature*, W.H. Freeman and Co., New York, 468 pp.

Mark, D.M., and P.B. Aronson, 1984. Scale Dependent Fractal Dimensions of Topographic Surfaces: An Empirical Investigation with Applications in Geomorphology and Computer Mapping, *Mathematical Geology*, 16:671–683.

Pecknold, S., S. Lovejoy, D. Schertzer, and C. Hooge, 1997. Multifractals and Resolution Dependence of Remotely Sensed Data: GSI to GIS, *Scale in Remote Sensing and GIS* (D.A. Quattrochi and M.F. Goodchild, editors), CRC Press, Boca Raton, Florida, pp. 361–394.

Quattrochi, D.A., 1993. The Need for a Lexicon of Scale Terms in Integrating Remote Sensing Data with Geographic Information Systems, *Journal of Geography*, 92(5):206–212.

Quattrochi, D.A., N.S.N. Lam, H. Qiu, and Wei Zhao, 1997. Image Characterization and Modeling System (ICAMS): A Geographic Information System for the Characterization and Modeling of Multiscale Remote Sensing Data, *Scale in Remote Sensing and GIS* (D.A. Quattrochi and M.F. Goodchild, editors), CRC Press, Boca Raton, Florida, pp. 295–308.

Walsh, S.J., A. Moody, T.R. Allen, and D.G. Brown, 1997. Scale Dependence of NDVI and its Relationship to Mountainous Terrain, *Scale in Remote Sensing and GIS* (D.A. Quattrochi and M.F. Goodchild, editors), CRC Press, Boca Raton, Florida, pp. 27–56.

Woodcock, C.E., and A.H. Strahler, 1987. The Factor of Scale in Remote Sensing, *Remote Sensing of Environment*, 21:311–312.